Numerical Evaluation of Main Rotor Pylon Flowfields on the RAH-66 Comanche Helicopter

Earl P.N. Duque
Research Scientist
Army/NASA Rotorcraft Division
US Army Aeroflightdynamics Directorate, AVRDEC, AMCOM
Ames Research Center
Moffett Field, CA

Edward T. Meadowcroft
Technical Specialist
Boeing U.S. Army Programs and Military Rotorcraft
Philadelphia, PA

Abstract

Steady-State and unsteady Reynolds-Averaged Navier-Stokes computations were used to evaluate main rotor pylon flowfields on the RAH-66 Comanche Helicopter. The computations were used in conjunction with wind tunnel and flight test experiments and focused on the effect of flow control devices and vehicle contours on tail buffet. The computations helped to give further insight into the phenomenological behavior of the flow control device.

Introduction

Tail buffet is the adverse coupling of unsteady flow field pressure frequencies and amplitudes surrounding the helicopter tail, with the tail structure natural frequencies. Tail buffet potentially causes exceedence of tail structural load limits, unacceptable vibration, and degraded handling qualities. Resolution of tail buffet usually focuses on reducing the flow field unsteady pressure amplitudes and modifying the frequency response of the tail structure. Although this phenomenon has been observed in many aircraft, designers do not completely understand what causes tail buffet. Each new design or design change can often result in a different buffet issue.

Presented at the AHS 55th Annual Forum and Technology Display May 25-27, 1999, Montreal, Canada.

The highly separated and unsteady flowfield emanating from behind a helicopter's main rotor hub and the flow from its main rotor pylon can have a large effect on tail buffet. In particular, the shape of the pylon and the installation of various flow control devices determine the interaction between these two regions. One such passive flow control device is known as a flow splitter. Many helicopters from various manufacturers utilize flow splitter devices. One can see similar devices on the Kiowa-Warrior OH-58D, the Chinook CH-47, and the Dauphin SA-365. The Comanche RAH-66 helicopter in particular has a flow splitter device installed on top of its main rotor pylon as shown by Fig. 1.

Wilson and Ahmed gave a phenomenological account of the fluid mechanics behind a similar configuration[1]. Specific to the RAH-66, the flow splitter is effectively a low aspect ratio flat plate that generates a coherent vortex structure along its lower surface. This vortex convects downstream beneath

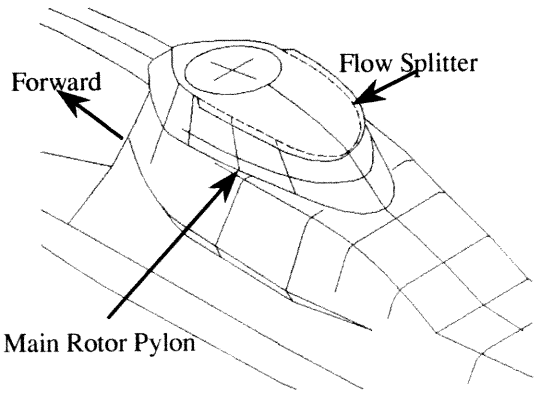

Figure 1 - Line drawing of rotor pylon with flow splitter

the splitter surface and along the pylon side. Its path and vorticity combine to prevent the pylon flow from detaching. Additionally, it is surmised that the splitter helps to segregate the mean flow into two regions: a separated flow region resulting from the main rotor hub that convects downstream along the top of the pylon and an attached flow region along the side of the main engine pylon. The overall shape of the main rotor pylon also has a great effect on tail buffet. The shape controls the location of separation and the inherent unsteady nature of the separation. To come upon a pylon shape optimized for aerodynamics, current designs rely upon a designer's extensive experience coupled with an extensive wind tunnel and flight test modeling effort.

The RAH-66 Comanche helicopter manufactured by the Boeing/Sikorsky team is the most recent aircraft destined for use by the U.S. Army. Since first flight in January 1996, the aircraft has gone through extensive flight tests. Along with the many successes, the flight tests revealed a tail-buffet phenomenon. As a result, an extensive wind tunnel and flight test program was initiated that involved the use of the Langley 14-by-22-foot Wind tunnel, the Sikorsky Pilot 4-by-6 foot Wind tunnel, the Boeing-Philadelphia 20-by-20 foot Wind tunnel, and flight tests of aircraft #1. The main goal of this effort was to determine the sources of tail buffet and to determine methods to alleviate any adverse effects.

In addition to the experiments, a numerical modeling effort was pursued. The goal of the numerical effort was to provide additional insight to the experiments. A number of computations were performed that explored a number of configuration changes and flight conditions. These computations in conjunction with the experimental results give a more complete understanding of the initial formation of vortices at the flow splitter and explain how they may interact with aerodynamic control surfaces downstream.

This paper documents the effects of the main rotor pylon on tail buffet and focuses primarily on the insight to the phenomenon as determined by the computations. To accomplish these goals, we first describe the methodologies used in the study along with a summary of the flow solver features. Then, the fidelity and accuracy of the steady-state Computational Fluid Dynamic (CFD) solutions are verified by comparing a baseline solution to flight test data and available wind tunnel data. We then present comparisons of computed steady-state flowfields with and without a flow splitter to demonstrate the device's effect on the local flowfield. Finally, unsteady CFD solutions give a detailed picture of the vehicle's wake and its impact on buffet frequencies. In summary, this paper demonstrates the constructive use of CFD during a vehicle design effort. It gives the rotorcraft community a better understanding of tail buffet sources and possibly better insight into how to prevent its occurrence.

Methodology

Steady-state (SSCFD) and unsteady (USCFD) solutions of the Comanche were obtained using two different versions of Buning's[2] OVERFLOW code. Steady-state solutions were obtained using OVERFLOW version 1.6. This code uses overset grids to discretize the flowfield of complex geometries and has a number of solver options. For the SSCFD studies, the scalar penta-diagonal method by Pulliam and Chausee[3] was used to advance the solution to convergence along with central

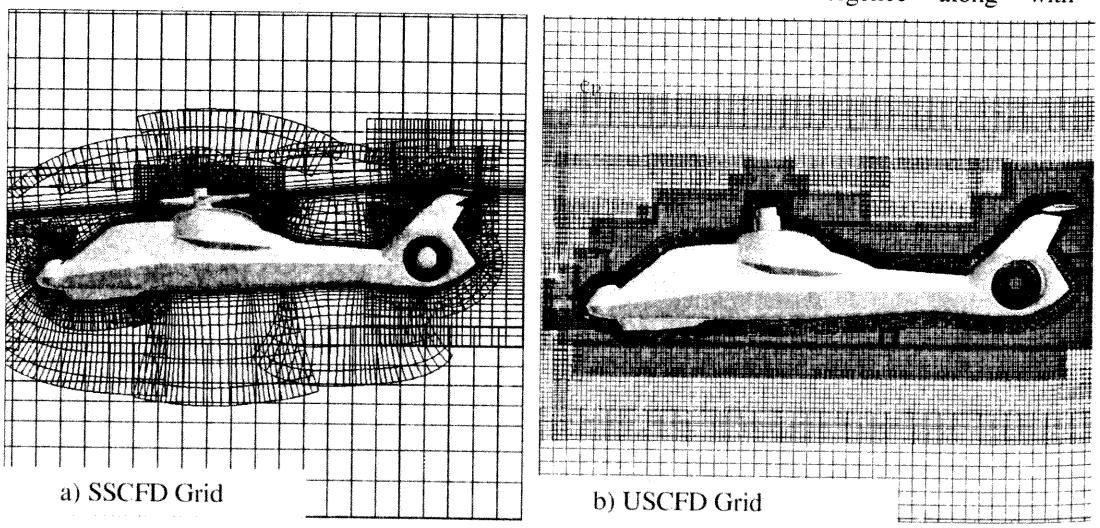

a) SSCFD Grid b) USCFD Grid

Figure 2 - Comanche overset grid

differences for the spatial differences. For stability, 2nd and 4th order central difference dissipation was used. The code uses a uniform pressure jump actuator disk to model rotor inflow for both the main rotor and fantail. A fully turbulent boundary layer was modeled using the Baldwin-Barth[4] model.

The USCFD solutions were obtained using a scalable version of OVERFLOW developed by Meakin and Wissink[5]. The scalable version of the OVERFLOW code was run using the block-tridiagonal Beam-Warming scheme[6] to advance the solutions in time. The USCFD results do not include the main rotor actuator disk. Meakin added algorithms to the code that facilitate grid adaptation in response to arbitrary relative motion between grid components and to evolving off-body flow dynamics.[7] Wissink and Meakin extended the methodology to allow the code to make efficient use of scalable parallel computer architectures such as the IBM SP2 and the Silicon Graphics Origin 2000.[8]

Furthermore, this version of the code know as OVERFLOW-D2 makes use of a large number of near body grids to discretize the geometry along with an extensive network of off-body uniform Cartesian background grids. This grid technique helps to improve grid resolution for off-body flows by maintaining grid resolution and quality. The large number of overset grids can help to evenly distribute the computational workload over a parallel computer's available processors.

Although both the SSCFD and USCFD use overset grid methods, their gridding schemes lead to some very different grid geometry and sizes. Both grids are on the order of seven million grid points.

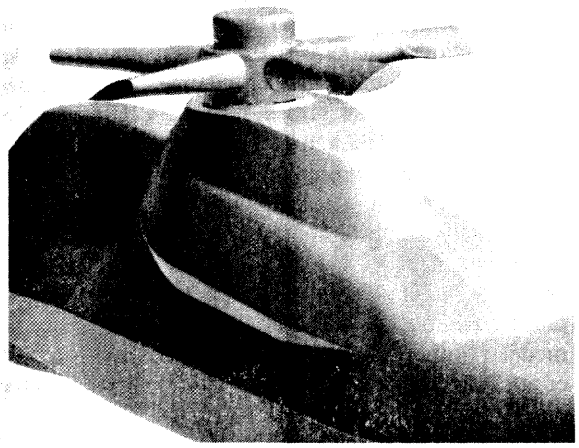

a) SSCFD baseline configuration

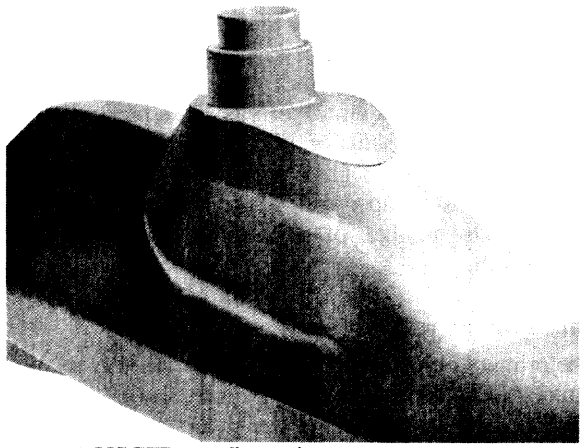

c) USCFD configuration

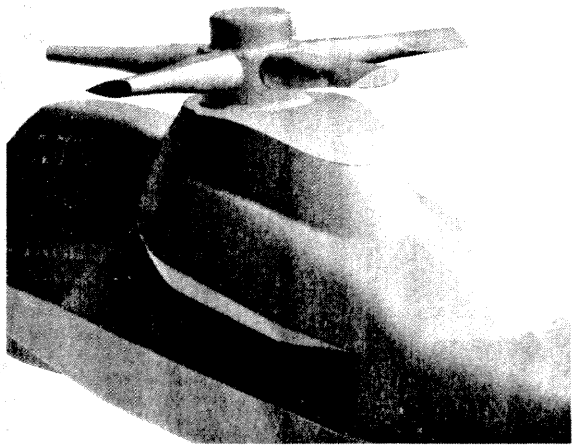

b) SSCFD baseline + flow splitter

Figure 3 - Pylon configurations

However, the USCFD grid system consists of 343 individual over grids while the SSCFD grid system consists of 48 individual grids, see Duque[9]. Fig. 2 compares the overset grid systems for the two methods.

Results and Comparisons

The computations were performed either before or during the wind tunnel experiments. This situation created a rare occasion where CFD solutions were required to provide timely information before an experiment. Each test required either specific configurations or specific flow conditions. Of the many configurations evaluated both experimentally and computationally, only results from the three illustrated in Fig. 3 will be presented:

a) SSCFD Baseline configuration
b) SSCFD Baseline + flow splitter configuration
c) USCFD configuration

Computed flow conditions correspond to forward flight speeds of 150 knots (Mach number = 0.21) at 0° and 6° angle of attack and 0° of yaw. The pressure jump applied to the actuator disk for the SSCFD results correspond to the gross weight of the flight vehicle. Reynolds number was set to the full-scale flight Reynolds number of 46 million based on fuselage length.

Baseline solution verification

The primary objective of this investigation was to determine tail buffet sources. Experiment shows that interference from the main rotor and pylon causes tail buffet at certain flight attitudes. The bulk of experimental wind tunnel data shows the effect of main rotor and pylon configuration changes on the measured unsteady flow fields and airloads at the tail.

As part of this exercise, one must determine the CFD method's ability to accurately predict the flowfield of the baseline aircraft. One must however make a distinction between verification and validation. Validation is a study that involves detailed quantitative comparisons between experiment and computed CFD results. On the experimental side, it requires that one document the accuracy and uncertainty of the results. On the CFD side, one must show a systematic grid refinement study that demonstrates grid independent solutions.

Solution verification is not as rigorous as a validation effort. It involves qualitative comparisons of computed and experimental results that verify that the CFD gives similar results. It does not usually involve a grid refinement study. Therefore, according to the above definitions, the CFD results for the current study will be "verified" by making some flowfield comparisons between SSCFD solutions and experiments.

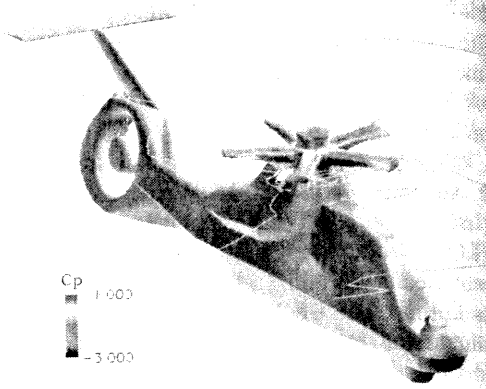

Figure 4 – SSCFD surface pressure coefficient contours on baseline configuration

Fig. 4 illustrates a solution obtained for Configuration 1. The grid for Configuration 1 was based upon an earlier grid system developed by Duque et.al. [10]. That grid system was based on the Langley 15% model and lacked the details of a flow splitter or main rotor hub.

The current configuration includes a representative hub and geometrically accurate blade shanks to 20% rotor radius. This SSCFD baseline grid system contains 48 sub-grids and 7 million grid points. Although the method had the capability to model both main and tail rotor thrust, all computations were performed with zero tail rotor

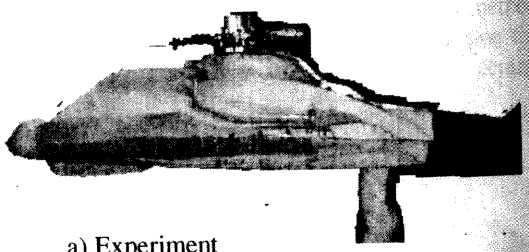

a) Experiment

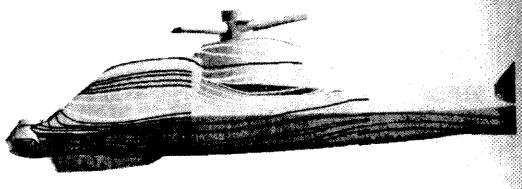

b) SSCFD

Figure 5 - Simulated oil flows

thrust.

The main rotor in the SSCFD solution was modeled via a uniform pressure jump actuator disk from 20 to 100% rotor radius. This model produced reasonable drag on the hub and inboard portion of the rotor with representative lift on the outboard portion. The model lacks rotor swirl and time dependent induced velocities, which are important components for modeling the pylon and rotor wake trajectories and their influence on the tail.

Previous work by Duque et.al.[10], showed comparisons with some wind tunnel surface pressures. Surface oilflows comparisons in Fig. 5 show further agreement between computation and experiment. The largest discrepancy occurs towards the aft end of the tail boom: On the test article, the flow is shown to strongly deflect downward. This difference may partially be due to the influence of the test support strut, which represents an obstacle to the surrounding flow.

Further comparisons of SSCFD and experiment global flowfield quantities gives further insight into the predicted flow field. Evaluating the accuracy of the SSCFD solution at the tail plane indirectly assessed the accuracy of the SSCFD at the main rotor and pylon. In the following comparisons of the flow field at the tail, the test article had the tail and fantail removed while the SSCFD had the tail and fantail present. Fig. 6 compares dynamic pressure magnitude, q, at the tail plane for test and SSCFD. At the horizontal tail location, both the test data and SSCFD show a region of high q flow due to the main rotor wake. At the vertical tail and fantail, the test data shows that the core of the q defect from the main rotor pylon strikes to the left and at the base of the vertical tail. The local dynamic pressure varies from 0.4 to 1.4 freestream q. The SSCFD shows the core to pass to the right of the tail. One explanation for this discrepancy between test and SSCFD is that the analysis predicts greater downwash from the advancing inboard section of the rotor, relative to the retreating side. This downwash deflects the rotor pylon wake to the left. Since the test configuration has greater inboard downwash than the SSCFD, the

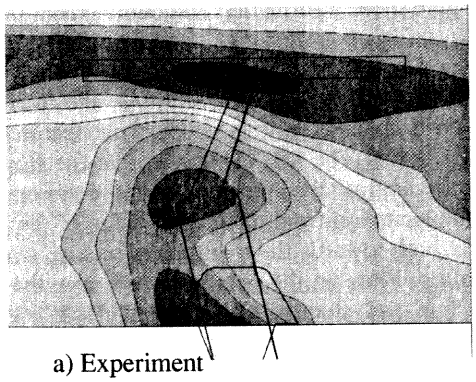

a) Experiment

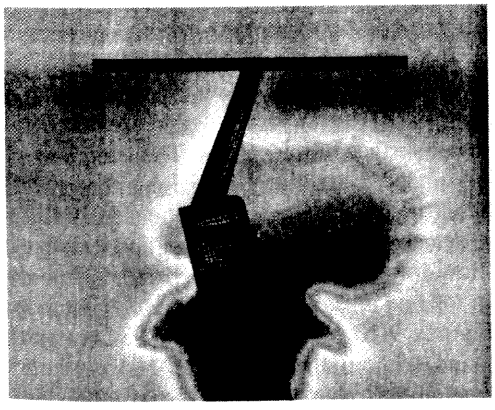

b) SSCFD

Figure 6 - Velocity contours at x-station 16000

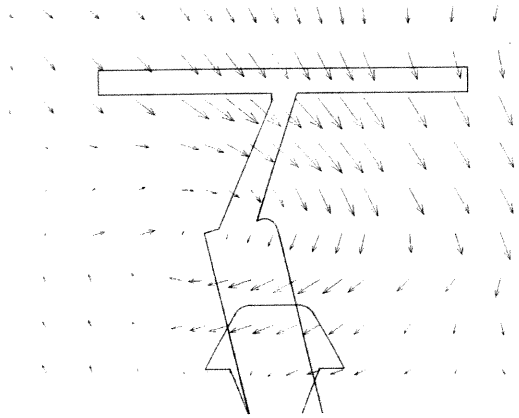

a) Experiment

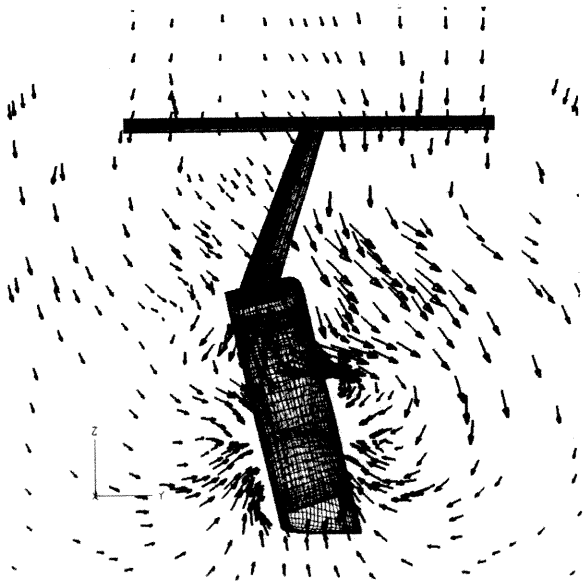

b) SSCFD

Figure 7 - Velocity vectors at x-station 16000

test wake should convect more to the left. Another reason is that loading on the vertical tail in the SSCFD model may cause the defect core to convect more to the right.

Fig. 7 compares time-averaged velocity magnitude and direction in the tail plane. Test data shows that the tail sees positive yaw flow angle on the upper portion and negative yaw flow angle on the lower, ranging from –4 to 14 degrees. These results indicate that rotor downwash and swirl may dominate. In comparison, the SSCFD seems to predict the uniform rotor downwash in the region of the horizontal tail and positive yaw sidewash over the entire span of the vertical tail. These results indicate that the rotor downwash and the presence of the tail dominate the flow.

Finally, Table 1 compares the time-averaged span loading on the vertical tail at 90% span as measured in the wind tunnel, flight test and obtained by the SSCFD. The wind tunnel data shows higher loading than the flight test. The CFD shows the lowest loading. The load is a function of the inflow magnitude and direction. In addition, the flow in the corner junction between the horizontal and vertical is separated due to mutual interference of the two surfaces. Test and CFD predict varying magnitudes for this separation.

Table 1 - Vertical tail load at 90% span
Local Force Coefficient (C_y) referenced to q_{inf}

Wind Tunnel	Flight Test	SSCFD
1.125	0.751	0.495

In summary, the verification effort shows that the SSCFD results can give a qualitative understanding of the resulting flowfield. The SSCFD captures a wake system that emanates from the main rotor pylon and interacts with the tail. Although the wake does not have the correct trajectory, the SSCFD method does capture the initial formation. With these limitations in mind, we now present results that illustrate the effect of the flow splitter on the local flowfield. We then show results from USCFD which give a more detailed picture of the unsteady rotor pylon wake.

Effect of splitters

Wind tunnel testing showed that the addition of the standard splitter to the baseline pylon reduced tail buffet at positive aircraft pitch angles with a small increase in buffet at negative pitch angles. Fig. 8 illustrates the splitter effect by comparing the difference between the root-mean-squared pressure acting on the right-hand and left-hand side of the vertical tail along a 7% chordwise location as a function of vehicle pitch and along several span

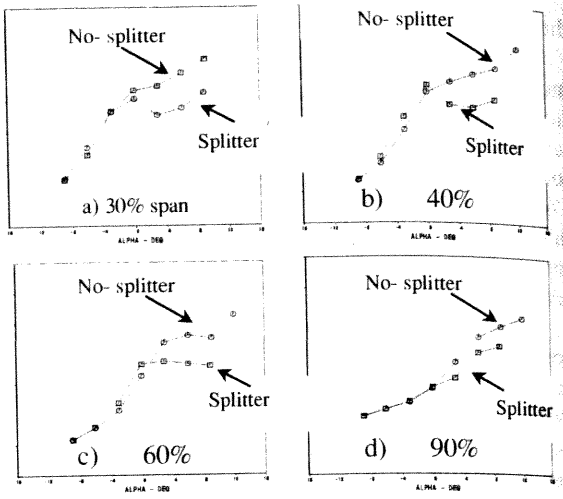

Figure 8 - RMS pressures from wind tunnel

locations. One can infer from Fig. 8 that the splitter plate helps to alleviate loads on the vertical tail at the higher pitch angles. At the same time, the tests measured no total drag increase. Although experiments show the flow splitter has an effect on tail loads, they do not fully explain how the splitter modifies the local flowfields. The results from the CFD give more information and complement the test data.

The SSCFD results do not directly predict tail buffet frequencies. They do show the effect of geometric changes on near body flow features that lead to buffet. The SSCFD shows that the flowfield from the area of the rotor and pylon convects such that the airstream from the leading edge of the pylon deflect both towards the pylon sides and up over the pylon top. Flow on the pylon top runs into the main rotor hub and shanks. This flow deflects over the rotor and back down the pylon sides with massive flow separation behind the rotor hub. Regions of separation also occur on the aft end of the pylon.

With the splitter installed, instead of deflecting from the rotor hub onto the pylon sides, the flow meets the upstream front edge of the flow splitter. Since the flow splitter is a low aspect ratio flat plate, it generates a coherent vortex structure that forms on the lower surface of the splitter. The generated vortex travels under the splitter and along the pylon side such that it prevents flow along the side of the pylon from detaching. Additionally, the splitter segregates the flow into two regions: a separated flow on the pylon top and an attached flow on the pylon side.

Figures 9,10 and 11 compare SSCFD solutions with and without the flow splitter along key cross sections of the vehicle. In these figures, the "Station" refers to station cut locations (in millimeters) along

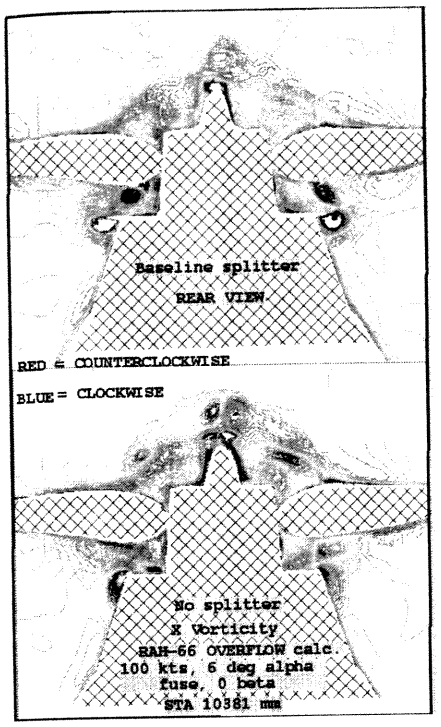

Figure 9 - Contours of X-component of vorticity at x-station 10381

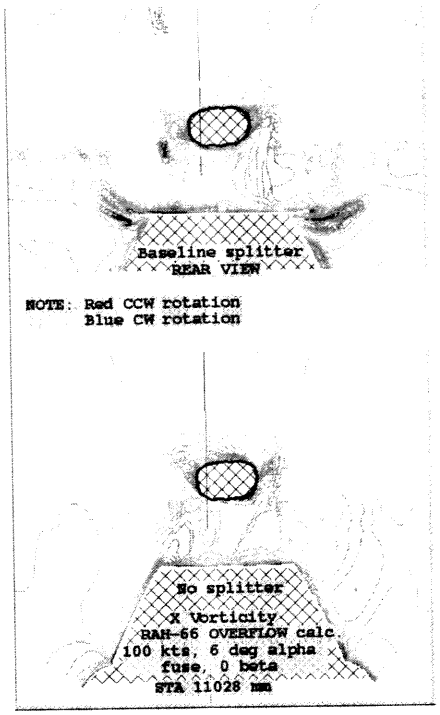

Figure 10 - Contours of X-component of vorticity at x-station 11028

the length of the vehicle as described in the air vehicle technical description[11]. The aircraft is pitched 6 degrees to amplify the splitter effect. Fig. 9 contains the X (streamwise) component of vorticity just past the hub center and clearly shows the formation of vorticity at the splitter leading edge. Fig. 10 shows the vorticity located at the aft end of the pylon. The splitter still generates vorticity, whereas the case without the splitter shows no significant vorticity. Fig. 11 contains the dynamic pressure at the aft end of the pylon. The no splitter case shows massive separation on the pylon top and sides. The flow in the splitter case shows a much smaller separation that remains confined to the pylon top. A small amount of separation persists on the underside of the splitter but does not seem excessive. This spillage may represent unrealized buffet reduction and suggests that a larger splitter may help to further reduce buffet.

In fact, subsequent design iterations of the splitter in wind tunnel tests converged on an optimized splitter that has larger planform area than the baseline analyzed here. Although still preliminary, the enlarged splitter seems to significantly reduce buffet and drag.

Although the SSCFD solutions can give some idea of a non-time varying flowfield, trying to extract information for an inherently unsteady phenomenon can yield erroneous conclusions. The captured vortex shedding and vortex street formations will not have correct frequencies and vortex trajectories in the far field. Vortex streeting is the phenomenon that occurs when flow separates behind objects of finite thickness; shedding of vorticity occurs, oscillating in time from one side to the other of the submerged object. The implementation of time accurate CFD calculations would enable the calculation of unsteady flow fields, including unsteady pressures that cause tail buffet. Unsteady CFD (USCFD) calculations would make it possible to analyze the direct impact of aircraft configuration changes on tail buffet. The expense of unsteady calculations impedes their use as they are an order of magnitude more expensive than their steady state counterparts.

Nevertheless, the limited use of USCFD solutions gives some insights into the dynamic time accurate behavior of the Comanche flowfield. As shown in Fig. 3, the configuration consisted of the baseline pylon and rotor hub with the splitter plate. The calculation was initiated from an impulsive start. The simulation consisted of 0.8 sec., full scale, time lapse. At 100 knots airspeed, this elapsed time allows the flow to convect the equivalent of 3 vehicle lengths during the simulation - a very limited time sample from which to draw many conclusions.

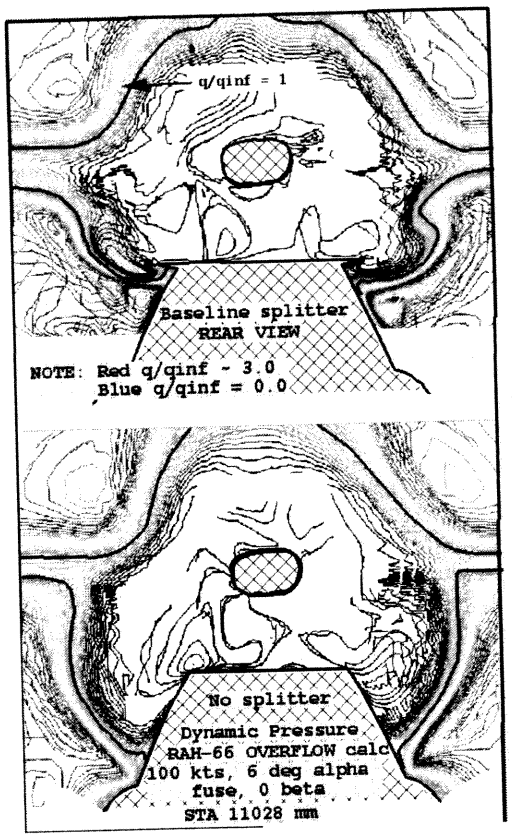

Figure 11 - Contours of q defect

Although the time sample is limited, the flow field visualizations of the unsteady flowfield do give further insight to the complex fluid dynamic interactions at the main pylon and their impacts on tail buffet. Fig. 12 presents a top and side view of the aircraft with streakline particles that originate from the main rotor pylon and convect to the base of the vertical tail. In the figure, the particles are colored by the time step at which they were released into the flow field. The blue particles represent the oldest particles; while the red particles represent youngest. Particles were released at four locations, which

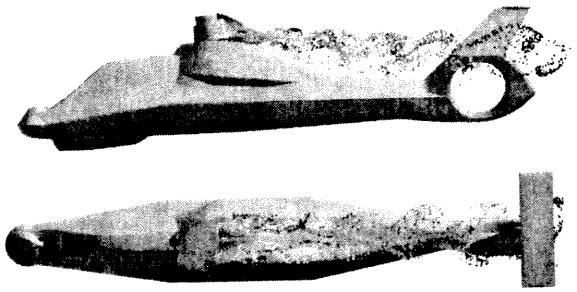

Figure 12 – Streak Particle from main rotor pylon

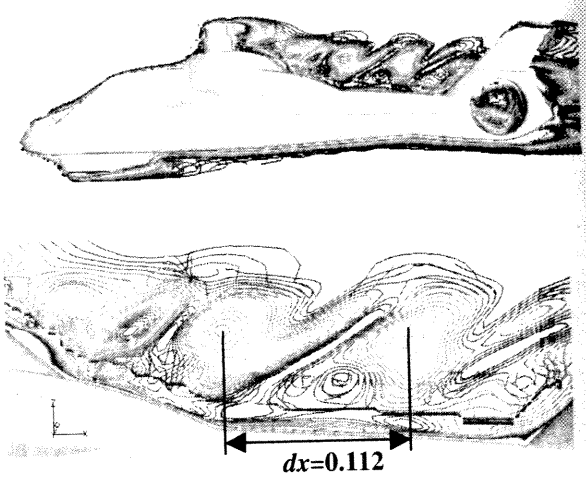

Figure 13 - Vorticity contours on aircraft symmetry plane

correspond to the dominant vortex cores that formed from the top of the hub and along the lower surface of the flow splitter. As shown by the top view, the particles emitted from the hub tend to spill over the top of the engine pylon and then flow outward to combine with the flow splitter particles.

The USCFD captures a complex vortex street that correlates to at least one of the measured dominant tail buffet frequencies. Fig. 13 illustrates vorticity contours along a cut-plane through the aircraft's symmetry plane. The full-length picture shows that the vortex street forms from a roll up of vorticity emitted from the top of the hub. This vorticity combines with shed vorticity from the rear of the splitter plate and rolls up into a street of coherent vortices. A normalized distance, dx, as shown separates these vortices. The local normalized vortex convection speed is approximately 0.11 which corresponds to a frequency of 25 Hz.. Fig. 14 shows the flight test pressure power spectral density versus

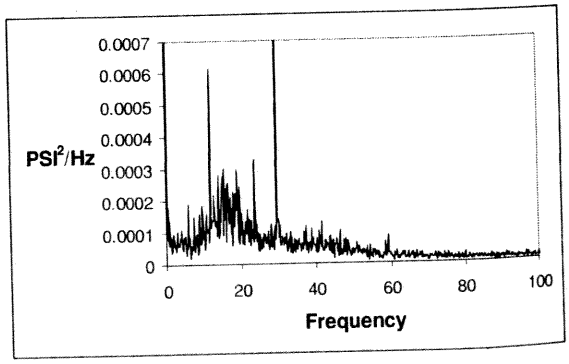

Figure 14 – Pressure power spectral density at specific location on tail

frequency for a representative location on the vertical tail. It shows pressure oscillations in the 5 – 25 Hz. range that couple with the structural dynamics to cause tail buffet. The frequency derived above falls within this frequency band. A more complete analysis, i.e. Fast Fourier Transform, of the complete pressure time history of the USCFD solution along with a longer computational run time are required to detect all the frequency content.

Conclusions

Steady-state and unsteady Reynolds Averaged Navier-Stokes simulations of the RAH-66 Comanche helicopter flow field were used to understand the effects of flow splitters on tail buffet. In general, the numerical method captures some aspects of vehicle aerodynamics as compared to test. Furthermore, the predictions of the splitter plate effect helped engineers to understand data acquired in tests. Comparisons of steady-state configurations with and without a flow splitter device gave further insight into the flowfield and the mechanisms that can lead to tail buffet on the Comanche helicopter. The simulations along with wind tunnel and flight tests helped engineers to decide upon design changes to the vehicle and resulted in changes to the splitter plate that are now undergoing flight tests. Overall, this paper demonstrates how one can use CFD methods in conjunction with tests and affect the design of current and future helicopters.

Acknowledgement

The authors would like to thank Dr. Robert L. Meakin of the US Army Aeroflighdynamics Directorate, Ames Research Center for providing his unsteady Comanche Simulation results that were generated as part of a DoD Common HPC Software Support Initiative (CHSSI) project.

References

[1] Wilson, F.T. and Ahmed, S.R., "Fuselage Aerodynamic Design Issues and Rotor/Fuselage Interactional Aerodynamics", AGARD Report No.781, Aerodynamics of Rotorcraft, pgs. 4.1 – 4.16, 1990.

[2] Buning, P., Chan, W., Renze, K., Sondak, D., Chiu, I., and Slotnick, J., OVERFLOW Users Manual ver 1.6ap, March 23, 1994.

[3] Pulliam, T.H. and Chaussee, D.S., "A Diagonal Form of an Implicit Approximate Factorization Algorithm, *Journal of Computational Physics*, Vol. 39, pgs. 347-363, 1981.

[4] Baldwin, B.S., and Barth, T.J., "A One-Equation Turbulence Transport Model for High Reynolds Number Wall-Bounded Flows," NASA TM 102847, 1990.

[5] Meakin, R.L., and Wissink, A.M., "Unsteady Aerodynamic Simulation of Static and Moving Bodies using Scalable Computers", To be presented at the 14th AIAA Computational Fluid Dynamics Conference, Norfolk, VA, AIAA-99-3302-CP, June 1999.

[6] Beam, R. and Warming, R.F., " An Implicity Finite-Difference Algorithm for Hyperbolic Systems in Conservation-Law Form", *Journal of Computational Physics*, Vol. 22, pp. 87-110, Sept. 1976.

[7] Meakin, R. "On Adaptive Refinement and Overset Structural Grids, AIAA-97-1858-CP, 13th AIAA Computational Fluid Dynamics Conference, Snowmass, CO, Jun 1997, pp.236-249.

[8] Wissink, A. and Meakin, R., "Computational Fluid Dynamics with Adaptive Overset Grids on Parallel and Distributed Computer Platforms, International Conference on Parallel and Distributed Processing, Las Vegas, NV, July 1998.

[9] Duque, E.P.N., and Dimanlig A.C.B, "Navier-Stokes Simulations of the RAH-66 (Comanche) Helicopter", Proceedings of the 1994 American Helicopter Society Aeromechanics Specialist Conference, San Francisco, CA, January 1994.

[10] Duque, E.P.N., Berry, J.D., Budge A.M. and Dimanlig, A.C.B., " A Comparison of Computed and Experimental Flowfields of the RAH-66 Helicopter", Proceedings of the 1995 American Helicopter Specialist Meeting, Fairfield County, CT., October 1995.

[11] Air Vehicle Technical Description, Boeing-Sikorsky Document number 2000-110-002, September 27,1993.